Inspiratory rhythmogenic activity is burst-independent and opioid-sensitive

Xiaolu Sun[1*], Carolina Thörn Pérez[1*], Nagaraj Halemani D[2], Xuesi M. Shao[1], Morgan Greenwood[3], Sarah Heath[1], Jack L. Feldman[1], and Kaiwen Kam[2,†]

[1]Department of Neurobiology, David Geffen School of Medicine at UCLA, Los Angeles, CA 90095, USA
[2]Department of Cell Biology and Anatomy, Chicago Medical School, Rosalind Franklin University of Medicine and Science, North Chicago, IL 60064, USA
[3]RFUMS/DePaul Research Internship Program, Rosalind Franklin University of Medicine and Science, North Chicago, IL 60064, USA

*Equal contribution

[†]Corresponding author and Lead Contact:
Kaiwen Kam, Ph.D.
Department of Cell Biology and Anatomy
Chicago Medical School
Rosalind Franklin University of Medicine and Science
3333 Green Bay Rd.
North Chicago, IL 60064-3095, USA
Email: kaiwen.kam@rosalindfranklin.edu
Phone: (847) 578-8630
Fax: (847) 578-3253

Summary

How mammalian neural circuits generate rhythmic activity in motor behaviors, such as breathing, walking, and chewing, remains elusive. For breathing, rhythm generation can be localized to a brainstem nucleus called the preBötzinger Complex (preBötC). Rhythmic preBötC population activity consists of small amplitude burstlets, which we hypothesize are rhythmogenic, and larger inspiratory bursts, which drive motoneuronal activity. If burstlets are rhythmogenic, opioids, analgesics that can cause profound respiratory depression, should similarly reduce burstlet frequency. In conditions where burstlets were separated from bursts in medullary slices from neonatal mice, the μ-opioid receptor (μOR) agonist DAMGO decreased burstlet frequency. DAMGO-mediated depression was abolished by genetic deletion of μORs in a glutamatergic preBötC subpopulation and was reduced by Substance P, but not blockade of inhibitory synaptic transmission. Our findings suggest that rhythmogenesis need not rely on strong bursts of activity associated with motor output and point to strategies for ameliorating opioid-induced depression of breathing.

Keywords: opioids, breathing, rhythm generation, central pattern generator

Introduction

Rhythmic motor behaviors in mammals, such as breathing, walking, and chewing, are controlled by neural circuits that determine the period of the movement and shape the pattern of motor activity. Despite the apparent simplicity of the computation, the mechanisms underlying rhythmogenesis in these circuits are unknown. Generation of breathing rhythm is localized to a compact nucleus in the ventrolateral medulla, the preBötzinger Complex (preBötC; Smith et al., 1991). In particular, two overlapping subpopulations of glutamatergic preBötC neurons, those expressing the neurokinin-1 receptor (NK1R) and those derived from progenitors that express the transcription factor Dbx1 (Dbx1^{+}), are necessary for inspiratory rhythmogenesis (Bouvier et al., 2010; Gray et al., 2010; Gray et al., 2001).

Until recently, rhythmic bursts of preBötC population activity were considered unitary events that determined both the timing and pattern of periodic inspiratory movements. However, we recently showed that these preBötC bursts consist of two separable components: i) large amplitude inspiratory bursts that are transmitted via premotoneurons to inspiratory motoneurons to activate muscles that produce inspiratory airflow; and ii) low amplitude burstlets that appear as preinspiratory activity when preceding these bursts and are not normally seen in motor nerve or muscle activity (Kam et al., 2013a). Because preBötC rhythmic activity can consist solely of burstlets that do not produce motoneuronal output, we hypothesize that burstlets are rhythmogenic (Kam et al., 2013a). A strong prediction of this hypothesis is that manipulations that affect inspiratory burst frequency should have similar effects on preBötC burstlet frequency.

To test this prediction, we examined the effects of opioids, analgesics that depress breathing at high doses, on bursts and burstlets and tested opioidergic interactions with other neurotransmitters and neuromodulators that affect preBötC neuronal excitability. We bath-applied [D-Ala^{2},N-MePhe^{4},Gly-ol^{5}]-enkephalin (DAMGO), a potent synthetic μ-opioid receptor (μOR) agonist, in conditions of low excitability *in vitro* when burstlets appeared at times bursts would have been expected or when preBötC rhythmic activity consisted solely of burstlets. We measured the frequency of inspiratory-related preBötC population activity, i.e., the intervals

45 between successive bursts or burstlets, to assay opioidergic effects on rhythmogenesis and
46 calculated the fraction of rhythmic preBötC events that were burstlets to assay changes in the
47 pattern-generating threshold mechanism that converts burstlets into bursts. We conclude that
48 DAMGO depresses inspiratory frequency by acting on burstlet producing preBötC Dbx1$^+$
49 neurons. These data are consistent with our hypothesis of distinct rhythm and pattern
50 generating mechanisms within the preBötC, with rhythmogenesis being mediated by burstlets
51 and a separable burst-generating mechanism governing patterned preBötC output. Our results
52 also inform potential approaches for combating opioid-induced depression of breathing.

53 **Results**

54 **DAMGO slows preBötC rhythmic activity without affecting burstlet fraction.**

55 Systemic administration of opioids slows breathing *in vivo* and *in vitro* (Boom et al., 2012; Gray
56 et al., 1999). We investigated how preBötC burstlets and bursts mediate these opioidergic
57 effects in neonatal mouse tissue slices that contain the preBötC and the hypoglossal motor
58 nucleus and nerve (XII) and generate a physiologically relevant motor output, i.e., inspiratory-
59 related rhythmic activity. Under baseline conditions in artificial cerebrospinal fluid (ACSF)
60 containing 9 mM K^+ and 1.5 mM Ca^{2+} ("9/1.5"), preBötC population activity and XII activity
61 consisted primarily of coincident, large amplitude rhythmic bursts (Fig. 1A; Smith et al., 1991).
62 Subsaturating concentrations of DAMGO caused a dose-dependent decrease in the frequency
63 (*f*) of rhythmic preBötC and XII bursts (Fig. 1A-C). 10 nM DAMGO significantly decreased
64 preBötC *f* from 0.22 ± 0.05 Hz to 0.13 ± 0.04 Hz (p=0.01, n=6; Fig. 1C). 30 nM DAMGO
65 application further decreased preBötC *f* to 0.07 ± 0.04 Hz (p=0.0001, n=6; Fig. 1C), and 100 nM
66 DAMGO led to complete cessation of XII activity and, in some cases, also blocked all preBötC
67 activity (Fig. 1B).

68 We previously showed that changes in XII *f* induced by decreases in extracellular K^+ could be
69 caused by a reversion of preBötC bursts to preBötC burstlets (Kam et al., 2013a). This was not
70 the case for the effects of DAMGO on *f*, as the fraction of total preBötC events that were
71 burstlets (burstlet fraction), which was very low in control conditions (0.14 ± 0.14), was not

72 significantly different from that in the presence of 30 or 100 nM DAMGO (p=0.8, n=6; Fig. 1A,
73 C). Moreover, the amplitude of preBötC bursts (0.60 ± 0.10 a.u.) was not significantly different
74 between control conditions without DAMGO and when 10 nM (0.61 ± 0.13 a.u.) or 30 nM
75 DAMGO (0.56 ± 0.19 a.u.) was added to the bath (p=0.8, n=6).

76 To determine whether DAMGO could affect the conversion of burstlets into bursts when the
77 preBötC was operating in a different dynamic mode, we decreased ACSF K^+ and Ca^{2+}
78 concentrations (Kam et al., 2013a). In 3 mM K^+ and 1 mM Ca^{2+} ("3/1"), preBötC activity was a
79 mixed pattern of burstlets and bursts (Fig. 1D, upper traces). While the burstlet fraction under
80 these conditions (0.58 ± 0.26) was significantly higher than that in 9/1.5 ACSF (0.14 ± 0.14;
81 p=0.003, n= 6 for 9/1.5, n=7 for 3/1), preBötC *f* was similar (0.23 ± 0.10 Hz in 3/1 vs. 0.22 ± 0.05
82 Hz in 9/1.5; p=0.8, n= 6 for 9/1.5, n=7 for 3/1; Fig. 1C, F). XII *f* in 3/1 ACSF (0.08 ± 0.05 Hz), on
83 the other hand, was significantly lower than XII *f* in 9/1.5 ACSF (0.2 ± 0.06 Hz; p=0.002, n= 6 for
84 9/1.5, n=7 for 3/1; Fig. 1B, E), a consequence of the increased fraction of preBötC burstlets that
85 were not transmitted to XII output.

86 In 3/1 ACSF, DAMGO decreased preBötC *f* in a dose-dependent manner, similar to its effects in
87 9/1.5 ACSF. Addition of 30 nM DAMGO significantly reduced preBötC *f* from 0.22 ± 0.1 Hz to
88 0.04 ± 0.04 Hz (p=0.001, n=7; Fig. 1D-F). This reduction was not significantly different from the
89 effects of 30 nM DAMGO in 9/1.5 ACSF (p=0.2, n=6 for 9/1.5, n=7 for 3/1; Fig. 1C, F). Higher
90 concentrations of DAMGO (≥100 nM) frequently blocked all preBötC population activity.
91 Burstlet and burst amplitudes in 3/1 ACSF (burstlet: 0.38 ± 0.05 a.u.; burst: 0.73 ± 0.08 a.u.) did
92 not change significantly when 10 nM DAMGO (burstlet: 0.36 ± 0.04 a.u.; burst: 0.78 ± 0.10 a.u.)
93 or 30 nM DAMGO (burstlet: 0.34 ± 0.11 a.u.; burst: 0.65 ± 0.21 a.u.) was bath-applied (burstlet:
94 p=0.7, burst: p=0.3, n=7), and the burstlet fraction was again unaffected by DAMGO (p=1.0,
95 n=7; Fig. 1F).

96 To determine whether opioids specifically affected rhythmogenic activity independent of burst
97 production, we isolated burstlets using low concentrations of Cd^{2+} (6-25 µM; Kam et al., 2013a),
98 which significantly increased the burstlet fraction from 0.42 ± 0.30 to 0.78 ± 0.20 (p=0.02, n=8)
99 without significantly changing preBötC *f* or amplitude (*f*: p=0.7, amplitude: p=0.06, n=8; Fig. 2A,

100 B). The decreases in excitability and synaptic efficacy caused by Cd^{2+} (Kam et al., 2013a; Lu et
101 al., 2007) resulted in an increased sensitivity to DAMGO. Bath application of 1 nM DAMGO on
102 this burstlet only rhythm was sufficient to abolish preBötC rhythmic activity completely in 7 of 8
103 slices. Concentrations of DAMGO below that causing rhythmic cessation (0.01-10 nM) slowed
104 preBötC *f* significantly from 0.28 ± 0.09 Hz to 0.18 ± 0.07 Hz (p=0.001, n=8; Fig. 2A, B). This
105 relative decrease in preBötC *f* (0.66 ± 0.16) was not significantly different from the effect of 10
106 nM DAMGO on preBötC *f* in 3/1 ACSF with no Cd^{2+} (0.63 ± 0.16; p=0.8, n=5 for 3/1, n=8 for
107 Cd^{2+}). However, burstlet amplitudes in the presence of both Cd^{2+} and DAMGO (0.29 ± 0.08)
108 were significantly reduced compared to Cd^{2+} alone (0.35 ± 0.09; p=0.003, n=8; Fig. 2A, B).

109 Depression of preBötC burstlet *f* by μOR activation points to DAMGO modulating preBötC
110 rhythmogenic mechanisms. We previously hypothesized that the emergent rhythmogenic
111 processes that produce burstlets manifested as the latency in ectopic burst initiation following
112 targeted excitation of 4-9 preBötC inspiratory neurons, whose molecular identity was
113 unspecified (Kam et al., 2013b). Here, in slices from $Dbx1^{+}$ reporter (*Dbx1*^{cre}*;Rosa26*^{tdTomato})
114 mice, we targeted preBötC $Dbx1^{+}$ neurons for holographic photostimulation to determine if
115 opioids also modulate this rhythmogenesis-related process (Fig. 2C-F). In control 9/1.5 ACSF,
116 ectopic bursts were reliably elicited when 5-10 $Dbx1^{+}$ neurons were targeted (probability of
117 success: 0.86 ± 0.08, n=6; Fig. 2D). When a set of neurons that reliably resulted in bursts in
118 response to photostimulation in control conditions were then excited in 30 nM DAMGO, the
119 probability of eliciting a burst was reduced to 0.48 ± 0.25 (n=4; Fig. 2D, E). In 100 nM DAMGO,
120 the success rate decreased significantly as stimulation of the threshold set that had previously
121 reliably triggered bursts was further compromised and, in some cases, failed to trigger a single
122 burst (p=0.006, n=6; Fig. 2D, E). In 200 nM DAMGO, stimulation was unsuccessful at eliciting
123 bursts (p=0.0003, n=6; Fig. 2E). Importantly, the latency between laser stimulation and burst
124 initiation in the cases when bursts were triggered in DAMGO (157 ± 22 ms) was significantly
125 increased compared to that in baseline conditions (105 ± 24 ms; p=0.002, n=5; Fig. 2F).

126 **μOR-expressing $Dbx1^{+}$ neurons mediate the rhythmogenic effects of opioids.**

127 Which preBötC neurons does DAMGO target to depress inspiratory rhythm? We hypothesized

128 that DAMGO was acting on preBötC Dbx1^{+} neurons, which are essential for respiratory rhythm
129 generation (Bouvier et al., 2010; Gray et al., 2010; Wang et al., 2014) and contain μOR mRNA
130 (Hayes et al., 2017). We first sought to determine whether these neurons express μOR protein
131 using immunohistochemistry. In *Dbx1^{Cre};Rosa26^{tdTomato}* mice, μOR protein expression
132 overlapped with the spatial distribution of tdTomato-expressing Dbx1^{+} neurons in preBötC and
133 the adjacent intermediate band of the reticular formation (IRt; Fig. 3A) and was localized to
134 individual preBötC Dbx1^{+} neurons (Fig. 3B-C).

135 To test whether μORs in Dbx1^{+} neurons mediated DAMGO inhibition, we used a
136 *Dbx1^{Cre};Oprm1$^{fl/fl}$* mouse line (Weibel et al., 2013), in which μORs are genetically deleted in
137 Dbx1^{+} neurons. We first examined whether preBötC μOR expression was knocked down in P2
138 *Dbx1^{Cre};Oprm1$^{fl/fl}$* mice compared to their littermate controls (Fig. 3D-I). *Dbx1* is not expressed
139 postnatally (Bouvier et al., 2010; Gray et al., 2010), and NK1R protein is predominantly found in
140 neuronal processes (Tan et al., 2010) while NK1R mRNA is sparsely expressed in somata (Fig.
141 S1). We therefore localized preBötC using tachykinin precursor peptide (TAC1) expression,
142 which colocalizes with NK1R, ventral to nucleus ambiguus (NA) as a marker for preBötC (Fig. S1;
143 Hayes et al., 2017). To measure μOR and TAC1 expression, we performed fluorescence *in situ*
144 hybridization, which avoids the non-specific labeling that may occur with some μOR antibodies
145 (Schmidt et al., 2013) and allows localization of TAC1 expression to somata (Fig. S1). Abundant
146 (>15 puncta) TAC1 mRNA was found in larger neurons confined to the preBötC (somatic
147 diameter: 27.08 ± 4.3 μm, n=121). Choline acetyl transferase (ChAT) mRNA probes were used to
148 mark NA. In *Dbx1$^{+/+}$; Oprm1$^{fl/fl}$* control mice, μOR mRNA puncta colocalized with TAC1 and NK1R
149 mRNA in the preBötC (Figs. 3D-F, S1), recapitulating the immunohistochemical distribution of
150 Dbx1^{+} neurons in the Dbx1^{+} reporter mice (Fig. 3A-C). Compared with μOR expression in
151 *Dbx1$^{+/+}$; Oprm1$^{fl/fl}$* mice (Fig. 3D-F), μOR expression in *Dbx1^{Cre}; Oprm1$^{fl/fl}$* mice was reduced in
152 regions where Dbx1^{+} neurons are normally found (Fig. 3D, G) and significantly reduced in TAC1
153 positive preBötC neurons (p=0.01, *Dbx1$^{+/+}$; Oprm1$^{fl/fl}$*: H-score = 139.07 ± 39.33, n = 5; *Dbx1^{Cre};*
154 *Oprm1$^{fl/fl}$*: H-score= 47.98 ± 19.77, n=3; Fig. 3G-I).

155 Having confirmed a decrease in μOR expression in preBötC in *Dbx1^{Cre}; Oprm1$^{fl/fl}$* mice, we

156 determined whether the functional effects of DAMGO on preBötC rhythm were similarly
157 affected. In rhythmic tissue slices from *Dbx1*^{Cre}*; Oprm1*$^{fl/fl}$ mice bathed in 9/1.5 ACSF, 100 nM
158 DAMGO had little effect on preBötC *f* (p=0.2, n=9; Figs. 3J, S2). In contrast, bath-applied
159 DAMGO in *Dbx1*$^{+/+}$*; Oprm1*$^{fl/fl}$ cre-negative littermates reduced preBötC *f* significantly (p=0.01,
160 n=6; Fig. 3J).

161 **DAMGO-mediated depression is diminished by Substance P, but not blockade of inhibitory**
162 **synaptic transmission.**

163 The coexpression of μOR and NK1R in preBötC Dbx1^{+} neurons raises the possibility that NK1R
164 activation, which increases respiratory frequency in wild type rodents (Gray et al., 1999; Yeh et
165 al., 2017), could be effective in reducing the depressant effects of DAMGO. When applied
166 together in 3/1 ACSF, 30 nM DAMGO was much less effective in reducing rhythmic activity in
167 the presence of the NK1R agonist Substance P (SP; 500 nM), and preBötC *f* was not significantly
168 different from that in control 3/1 ACSF conditions, i.e., in the absence of SP and DAMGO
169 (p=0.09, n=6; Fig. 4A,C). We next tested whether altering preBötC excitability by blockade of
170 inhibitory synaptic transmission using a cocktail of the $GABA_A$ receptor antagonist picrotoxin
171 and the glycine receptor antagonist strychnine (picrotoxin/strychnine; Del Negro et al., 2009;
172 Ren and Greer, 2006; Shao and Feldman, 1997) would similarly block DAMGO-mediated
173 depression. In contrast to SP, picrotoxin/strychnine (100 μM/1 μM) did not reduce the effects
174 on preBötC *f* of 30 nM DAMGO compared to control conditions in either 9/1.5 or 3/1 ACSF
175 (p=0.2, n=6 for 9/1.5, n=7 for 3/1, n=13 for picrotoxin/strychnine; Fig. 4B, C). Indeed, preBötC *f*
176 when SP was applied with 30 nM DAMGO was greater than that in 9/1.5 ACSF, with or without
177 picrotoxin/strychnine, or 3/1 ACSF in the presence of DAMGO (p=0.001, n=6 for 9/1.5, n=7 for
178 3/1, n=12 for picrotoxin/strychnine, n=6 for SP; Fig. 4C).

179 Are the differential efficacies of SP and blockade of inhibitory transmission expressed in their
180 effects on baseline rhythmic activity? To determine how SP and blockade of inhibitory
181 transmission affect rhythm and pattern generation, we tested the effects of SP and
182 picrotoxin/strychnine on preBötC activity in 3/1 ACSF without DAMGO. Under these conditions,
183 bath-applied SP (500 nM) significantly reduced the burstlet fraction from 0.47 ± 0.3 to

184 0.10 ± 0.12 (p=0.01, n=6), but, surprisingly, did not affect preBötC *f* (p=0.4, n=6; Fig. 4D, E). In
185 slices from *Dbx1^{Cre}; Oprm1$^{fl/fl}$* mice bathed in 9/1.5 ACSF, we confirmed that 500 nM SP
186 significantly increased preBötC *f* (Fig. S2) and modulated preBötC *f* independent of μORs, which
187 were deleted in Dbx1^{+} neurons in these slices. In 3/1 ACSF, bath-applied picrotoxin/strychnine
188 (100 μM/1 μM) also significantly decreased burstlet fraction (p=0.0001, n=13) and did not alter
189 preBötC *f* significantly (p=0.9, n=13; Fig. 4F, G).

190 **Discussion**

191 Inspiratory rhythm generation must be both robust, to operate almost continuously throughout
192 the lifetime of the animal, and labile, to adapt to changing metabolic and environmental
193 conditions and coordinate with other behaviors. How the preBötC generates rhythm to meet
194 these challenges has thus far defied a thorough understanding. We put forth a hypothesis that
195 respiratory rhythmogenesis is driven not by strong bursts, but by preBötC burstlets (Fig. 4H;
196 Kam et al., 2013a). Burstlets occur when spontaneous firing among preBötC neurons reaches a
197 threshold for synchrony, and the time required for preBötC neurons to assemble and achieve
198 this synchrony (percolation) determines the period of the rhythm (Kam et al., 2013a; S.A. and
199 J.L.F., in preparation).

200 A strong prediction of this hypothesis is that manipulations that depress burst frequency should
201 also slow burstlet frequency. Indeed, we found that DAMGO specifically slowed preBötC *f*
202 without affecting burstlet fraction when the rhythm: i) was composed of mostly bursts; ii) was a
203 mixed pattern of bursts and burstlets; or iii) was mostly (or all) burstlets (Fig. 4H). Additionally,
204 DAMGO prolonged the latency between photostimulation and burst generation when threshold
205 sets of ≤10 neurons were excited. The congruent effects of DAMGO on both burstlet *f* and
206 photostimulation latency: i) is consistent with our hypothesis that both are products of
207 percolation of activity within the preBötC microcircuit, a critical process for rhythmogenesis
208 (Kam et al., 2013a; Kam et al., 2013b), and ii) suggests that DAMGO directly affects
209 rhythmogenic mechanisms.

210 Consistent with our functional studies, we found abundant μOR expression in preBötC Dbx1^{+}

211 neurons that form the core circuitry for inspiratory rhythmogenesis (Wang et al., 2014). We
212 also showed colocalization of μOR with NK1R in some preBötC neurons as well as with a
213 partially overlapping preBötC subpopulation expressing TAC1 that may be one endogenous
214 source of SP (Liu et al., 2004). When μORs were genetically deleted in Dbx1^{+} neurons in *Dbx1^{Cre};*
215 *Oprm1$^{fl/fl}$* mice, the potent rhythmic slowing effect of DAMGO in slices was no longer present.
216 These data suggest that μORs in preBötC Dbx1^{+} neurons mediate DAMGO inhibition of
217 rhythmicity.

218 How could μOR activation affect the percolation of activity in the preBötC that we hypothesize
219 underlies rhythmogenesis and transform, i.e., slow down, the dynamics of the Dbx1^{+} preBötC
220 network? μORs can be localized postsynaptically on dendrites and cell bodies, where they
221 regulate neuronal excitability and transduce receptor activation to downstream signal
222 transduction pathways; μORs are also found presynaptically on axon terminals where they
223 inhibit neurotransmitter release via activation of K^{+} conductances and/or inhibition of Ca^{2+}
224 conductances (Le Merrer et al., 2009; Mansour et al., 1988; Montandon et al., 2016; Williams et
225 al., 2001). We suggest that DAMGO-mediated hyperpolarization and/or decreases in synaptic
226 probability of release in and among μOR-expressing preBötC Dbx1^{+} neurons reduce
227 spontaneous firing rate, weaken the propagation of action potentials to postsynaptic neurons,
228 and increase the number of inputs required to reach action potential threshold. These effects
229 reduce the moment-to-moment probability that a critical number of neurons will be
230 simultaneously active and prolong the time required for preBötC neurons to increase their
231 firing, achieve synchrony, and generate burstlets (S.A. and J.L.F., in preparation).

232 The pattern-generating mechanism that converts burstlets to bursts may, by analogy, require a
233 higher threshold of activity and synchrony be reached via independently regulated, distinct
234 mechanisms, such as the activation of persistent inward conductances (Picardo et al., 2019).
235 Through this threshold mechanism, SP and blockade of inhibitory synaptic transmission
236 increase, whereas Cd^{2+} decreases, the fraction of preBötC events that are burstlets, without
237 altering frequency of these events (Fig. 4H). Interestingly, the depressant effects of DAMGO
238 were reduced by SP, but not inhibitory blockade. Inhibitory synaptic activity in preBötC is

239 dispensable for generation of breathing rhythm *in vivo* and *in vitro* (Janczewski et al., 2013;
240 Shao and Feldman, 1997) and has variable effects on excitability (Ren and Greer, 2006), which
241 may account for the inability of picrotoxin and strychnine to mitigate DAMGO-induced
242 depression. Alternatively, inhibition may act elsewhere in the microcircuit or upstream of
243 opioidergic signaling pathways within Dbx1$^+$ neurons.

244 While inhibitory blockade specifically affected pattern generation and was unable to rescue
245 DAMGO-mediated depression, NK1R activation seems capable of modulating both rhythm and
246 pattern in a state-dependent manner that can offset the effects of DAMGO (Fig. 4H). A ceiling
247 effect, i.e., preBötC *f* being near or at maximal, may have limited the rhythmogenic effect of SP
248 in 3/1 ACSF alone, but did reveal a pattern generating effect on burstlet fraction. Consistent
249 with SP effects in 9/1.5 ACSF (Gray et al., 1999; Yeh et al., 2017), co-application of opioids and
250 SP demonstrated a role for NK1R activation in modulating rhythm that is likely mediated by
251 intracellular interactions in preBötC Dbx1$^+$ neurons that coexpress μOR and NK1R. The μOR
252 expression and DAMGO sensitivity of NK1R-expressing neurons are well-documented (Gray et
253 al., 1999; Montandon et al., 2011), and G_s-protein coupled signaling of NK1R opposes the $G_{i/o}$-
254 coupled signaling of μORs (Gray et al., 1999; Johnson et al., 1996). However, the interaction of
255 NK1R and μOR can be complicated. Opioids may inhibit SP release, and SP potentiates the
256 antinociceptive effects of morphine through release of endogenous opioids (Fukazawa et al.,
257 2007; Kream et al., 1993). SP may also act directly on μORs as a weak agonist since naloxone,
258 the μOR antagonist, blocks SP excitation in some neurons (Davies and Dray, 1977).
259 Nonetheless, we predict that only neuropeptides and neuromodulators, whose receptors are
260 coexpressed with μORs in rhythmogenic preBötC neurons, like NK1Rs, are able to modulate
261 μOR signaling intracellularly to mitigate DAMGO-mediated depression.

262 The interaction between excitatory neuromodulatory systems with opiates in respiratory neural
263 circuits is relevant for addressing the depressive effects of opiates on breathing. Opioids are the
264 most commonly prescribed drugs for severe acute and chronic pain and play an important role
265 in palliative care. However, with a high potential for addiction, opiate overprescription and
266 abuse has created a pressing public health crisis that affects millions (CBHSQ, 2018). Morbidity

267 and mortality from opioid addiction and overdose is largely a result of opioid-induced
268 depression of breathing (Jaffe & Martin, 1990). Opiates given systemically will act on opioid
269 receptors throughout the nervous system (Kibaly et al., 2019), and μORs are expressed in
270 various brain structures regulating breathing (Gray et al., 1999; Manzke et al., 2003; Phillips et
271 al., 2012; Pokorski and Lahiri, 1981; Prkic et al., 2012; Zhang et al., 2007; Zhang et al., 2011).
272 While depression of breathing is unlikely to be dependent on actions at a single site (Lalley et
273 al., 2014; Montandon and Horner, 2014; Stucke et al., 2015), our data is consistent with
274 compelling *in vitro* and *in vivo* evidence that the preBötC is the most sensitive site to μOR
275 agonists and that it mediates respiratory frequency depression by opioids (Ballanyi and
276 Ruangkittisakul, 2009; Janczewski et al., 2002; Montandon and Horner, 2014; Montandon et al.,
277 2011).

278 In summary, the depressive effect of the μOR agonist DAMGO on preBötC burstlet frequency, in
279 the absence of a change in burstlet fraction, supports a primary role for burstlets in respiratory
280 rhythm generation and is consistent with the hypothesis that rhythm and pattern generating
281 mechanisms within the preBötC are separable. We propose that having distinct mechanisms
282 generating burstlets and bursts provides functional substrates for targeted modulation of the
283 rhythmic timing and/or pattern of breathing by other brain areas and neuromodulators. This
284 organization enables the dynamic temporal and pattern lability characteristic of breathing
285 essential for adaptation to changing metabolic demands and for coordination with other
286 respiratory-related and orofacial behaviors. A better understanding of the mechanisms of μOR
287 actions in respiratory neural circuits has important implications for developing stimulants that
288 excite breathing via non-opioidergic pathways (van der Schier et al., 2014) and drugs that
289 reverse opioid actions on preBötC Dbx1^{+} neurons to maintain breathing without affecting
290 analgesia.

291

292 **Acknowledgements**

293 The authors thank Grace Li for excellent technical work. *Oprm1*$^{fl/fl}$ mice were generously
294 provided by Dr. Wendy Weibel, Dr. Chris Evans, and the Animal Breeding Core (NIDA P50 Center

Grant, DA005010). This work was supported by National Institutes of Health grants NS07221, HL135779, and NS097492; and an international postdoctoral grant from the Swedish Research Council (Vetenskapsrådet).

Author contributions: X.S., J.L.F., and K.K. designed the research; X.S., C.T.P., N.H., X.M.S., M.G., S.H., and K.K. performed the research; X.S., C.T.P. and K.K. analyzed the data; X.S., C.T.P., J.L.F., and K.K. wrote the paper.

Declaration of Interests

The authors declare no competing interests.

305 **Figure legends**

306 **Figure 1. μOR activation depresses inspiratory frequency without affecting burstlet fraction.**
307 (A) Representative traces of ∫preBötC and ∫XII population activity in 9/1.5 ACSF control (ctrl)
308 and 30 nM DAMGO. Scale bar, 10 s.
309 (B) Representative time course of an experiment where increasing concentrations of DAMGO
310 were bath-applied in 9/1.5 ACSF. Interevent intervals (int.) in preBötC (top) and XII (bottom) are
311 plotted. In this experiment, 100 nM DAMGO led to cessation of rhythm.
312 (C) Average burstlet fraction and preBötC *f* in 9/1.5 ACSF (ctrl) and 10 nM and 30 nM DAMGO.
313 Increasing concentrations of DAMGO did not significantly affect burstlet fraction whereas
314 preBötC *f* was significantly lower in 10 nM and 30 nM DAMGO. *, $p < 0.05$, One-way ANOVA,
315 post-hoc Tukey test, n=6.
316 (D) Representative traces of ∫preBötC and ∫XII population activity in 3/1 ACSF control (ctrl) and
317 30 nM DAMGO. Both small amplitude burstlets (•), which did not produce XII activity, and large
318 amplitude bursts, which generated XII bursts, were observed. Scale bar, 10 s.
319 (E) Representative time course of an experiment, where increasing concentrations of DAMGO
320 were bath-applied in 3/1 ACSF. Interevent intervals in preBötC (top) and XII (bottom) are
321 plotted. In this experiment, 100 nM DAMGO led to cessation of XII activity while preBötC
322 rhythm persisted.
323 (F) Average burstlet fraction and *f* in 3/1 ACSF (ctrl) and 10 nM and 30 nM DAMGO. Increasing
324 concentrations of DAMGO did not significantly affect burstlet fraction whereas preBötC *f* was
325 significantly lower in 30 nM DAMGO. *, $p < 0.05$, One-way ANOVA, post-hoc Tukey test, n=7.

326 **Figure 2. DAMGO specifically modulates preBötC rhythmogenesis.**
327 (A) Representative traces of ∫preBötC and ∫XII population activity in 3/1 ACSF control (ctrl), 8
328 μM Cd^{2+}, and 8 μM Cd^{2+} + 10 nM DAMGO. In 3/1 ACSF (top), rhythmic activity consisted of both
329 burstlets and bursts. After Cd^{2+} application (middle), preBötC bursts were no longer observed,
330 and XII activity was abolished, leaving only a preBötC burstlet rhythm with a *f* similar to control.
331 With addition of DAMGO (bottom), burstlet *f* and amplitude decreased. Scale bar, 5 s.

332 (B) Average burstlet fraction, preBötC *f*, and burstlet amplitude (amp.) in 3/1 ACSF control (ctrl),
333 6-25 µM Cd^{2+}, and 6-25 µM Cd^{2+} + 0.1-10 nM DAMGO. Addition of Cd^{2+} significantly increased
334 the burstlet fraction while preBötC *f* and burstlet amplitudes were unchanged. Bath application
335 of DAMGO significantly decreased preBötC *f* (consisting almost solely of burstlets) and burstlet
336 amplitude. *, $p < 0.05$, One-way ANOVA, post-hoc Tukey test, n=8.
337 (C) Representative image of tdTomato fluorescence in the preBötC of a medullary slice from a
338 *Dbx1^{cre};Rosa26^{tdTomato}* mouse. Dashed circles represent holographic spots over targeted Dbx1^{+}
339 neurons. Scale bar, 20 µm.
340 (D) Overlays of representative traces of ∫preBötC from successive laser stimulations of the 8
341 Dbx1^{+} neurons shown in (C) in control 9/1.5 ACSF (ctrl), 30 nM DAMGO, and 100 nM DAMGO.
342 Arrow represents time of laser stimulation. In 9/1.5 ACSF, a failure was seen, but burst initiation
343 was otherwise reliably successful. Bursts were consistently triggered after a ~100 ms latency. In
344 30 nM DAMGO, failures were more frequent when the same stimulation parameters were
345 used, and the latency between laser stimulation and burst initiation was longer and more
346 variable. In 100 nM DAMGO, bursts were no longer triggered with the same stimulation
347 parameters. Scale bar, 200 ms.
348 (E) Average success rate (stim→burst) for burst initiation in control 9/1.5 ACSF (ctrl) conditions
349 and in increasing concentrations of DAMGO using entraining stimuli that elicits >80% success in
350 9/1.5 ACSF. To entrain the rhythm, 5-10 Dbx1^{+} neurons were stimulated 8 - 20 times every 3-6
351 s. DAMGO produced a dose-dependent decrease in the success rate for triggering bursts with a
352 significant reduction in success between control and at 100 nM and 200 nM DAMGO. *, $p <$
353 0.05, One-way ANOVA, post-hoc Tukey test, n=6.
354 (F) Average latency between laser stimulation and burst initiation when bursts were
355 successfully triggered during entraining stimuli was increased in 30 nM DAMGO compared to
356 control 9/1.5 ACSF (ctrl). *, $p<0.05$, Student's *t*-test, n=5.

357 **Figure 3. µORs expressed in Dbx1^{+} neurons mediate DAMGO inhibition of preBötC rhythmic**
358 **activities.**
359 (A) Confocal images of brainstem sections of a *Dbx1^{Cre};Rosa26^{tdTomato}* mouse pup (P2) double-
360 stained with antibodies to ChAT (blue) and µOR (green). Coronal sections showing µOR

361 expression in the preBötC and the Intermediate band of the Reticular Formation (IRt) and
362 colocalization with Dbx1^{+} neurons in the preBötC. Scale bar, 500 µm.
363 (B) Higher magnification of nucleus ambiguus (NA) and preBötC from the boxed region in A.
364 Scale bar, 50 µm.
365 (C) Expanded images of the boxed preBötC region highlighted in B. The arrow shows a preBötC
366 Dbx1^{+} neuron with abundant punctate µOR expression on the cell body. Scale bar, 10 µm.
367 (D) Confocal image of a medullary brainstem section at the level of the preBötC from a control
368 P2 *Dbx1$^{+/+}$; Oprm1$^{fl/fl}$* mouse processed with RNAScope. Probes for µOR (magenta), TAC1
369 (white), and acetylcholine esterase (ChAT; green) were used, and the tissue was counterstained
370 with DAPI (blue). A box marks the location of preBötC. Scale bar, 1 mm.
371 (E) Higher magnification of the boxed preBötC region in D. µOR and TAC1 were highly expressed
372 in this region. Scale bar, 100 µm.
373 (F) Higher magnification images of µOR-expressing neurons with (arrows) and without
374 (arrowhead) TAC1 expression from E. Colocalization of TAC1 and multiple µOR puncta was
375 observed in several neurons as well as abundant µOR puncta in neurons that did not express
376 TAC1. Scale bar, 40 µm.
377 (G) Confocal image of a medullary brainstem section at the level of the preBötC from a P2
378 *Dbx1$^{cre/cre}$; Oprm1$^{fl/fl}$* mouse processed with RNAScope. Probes for µOR (magenta), TAC1
379 (white), and acetylcholine esterase (ChAT; green) were used, and the tissue was counterstained
380 with DAPI (blue). In the preBötC of these mice, the density of µOR puncta was low. A box marks
381 the location of preBötC. Scale bar, 1 mm.
382 (H) Higher magnification of the boxed preBötC region in G. The density of µOR puncta was low,
383 and µOR expression was not associated with TAC1 expression. Scale bar, 100 µm.
384 (I) Higher magnification images of TAC1-expressing neurons from H with few to no µOR puncta
385 (arrows) as well as µOR-expressing neurons without TAC1 expression (arrowhead). Scale bar, 40
386 µm.
387 (J) Average *f* of preBötC activity in control 9/1.5 conditions (ctrl) and 100 nM DAMGO in
388 *Dbx1^{Cre}; Oprm1$^{fl/fl}$* mice (right), where µORs are selectively deleted in Dbx1^{+} neurons, and their
389 *Dbx1$^{+/+}$;Oprm1$^{fl/fl}$* littermate controls with preserved µOR expression (left). Whereas 100 nM

390 DAMGO reduced preBötC *f* significantly in *Dbx1*$^{+/+}$;*Oprm1*$^{fl/fl}$ control mice, the same
391 concentration had no effect on *f* when μORs were deleted. *, p<0.05, Student's *t*-test, n=6 for
392 *Dbx1*$^{+/+}$;*Oprm1*$^{fl/fl}$, n=9 for *Dbx1*^{Cre};*Oprm1*$^{fl/fl}$.

393 **Figure 4. Substance P, but not blockade of inhibitory synaptic transmission, relieves DAMGO-**
394 **mediated depression.**
395 (A) Representative traces of ∫preBötC and ∫XII population activity in 3/1 ACSF control (ctrl) and
396 500 nM SP and 30 nM DAMGO. SP mitigated the effects of DAMGO, and preBötC activity
397 resembled that in control conditions. Scale bar, 10 s.
398 (B) Representative traces of ∫preBötC and ∫XII population activity in 3/1 ACSF control (ctrl) and
399 100 μM picrotoxin/1 μM strychnine and 30 nM DAMGO. The addition of picrotoxin/strychnine
400 following DAMGO application did not recover preBötC *f* to control levels. Scale bar, 10 s.
401 (C) Average normalized *f* of preBötC activity when 30 nM DAMGO was added alone (9/1.5, 3/1)
402 or following application of either 500 nM SP or 100 μM picrotoxin/1 μM strychnine with 30 nM
403 DAMGO. For each experiment, values were normalized to preBötC *f* during baseline 9/1.5 or
404 3/1 ACSF in that experiment. When picrotoxin/strychnine were added with DAMGO, the
405 relative change in *f* did not differ from the normalized *f* when DAMGO was applied alone in
406 either 9/1.5 ACSF or 3/1 ACSF. The normalized *f* when SP was added with DAMGO was
407 significantly higher than all other conditions. *, p < 0.05, One-way ANOVA, post-hoc Tukey test,
408 n=6 for 9/1.5, n=7 for 3/1, n=12 for picrotoxin/strychnine, n=6 for SP.
409 (D) Representative traces of ∫preBötC and ∫XII population activity in 3/1 ACSF control (ctrl) and
410 500 nM SP. In 3/1 ACSF, rhythmic activity consisted of both burstlets and bursts. After SP, *f* was
411 unchanged, but more preBötC bursts were observed. Scale bar, 10 s.
412 (E) Average burstlet fraction and *f* in 3/1 ACSF control condition (ctrl) and 500 nM SP. SP
413 significantly decreased the burstlet fraction, but did not change preBötC *f*. *, p < 0.05, Student's
414 t-test, n=13.
415 (F) Representative traces of ∫preBötC and ∫XII population activity in 3/1 ACSF control (ctrl) and
416 100 μM picrotoxin/1 μM strychnine. In 3/1 ACSF, rhythmic activity consisted of both burstlets
417 and bursts. After picrotoxin/strychnine, *f* was unchanged; however, more preBötC bursts were
418 observed, and XII bursts were larger. Scale bar, 10 s.

419 (G) Average burstlet fraction and *f* in 3/1 ACSF control condition (ctrl) and 100 µM picrotoxin/1
420 µM strychnine. Picrotoxin/strychnine significantly decreased the burstlet fraction, but did not
421 change preBötC *f*. *, $p < 0.05$, Student's t-test, n=13.
422 (H) Model for preBötC rhythm and pattern generation. In the absence of neuromodulation
423 (center), rhythm generation is the alternation between burstlet activity and the silent
424 interburstlet interval (IBI). Pattern generation in the preBötC occurs when burstlet activity
425 reaches a threshold (dashed line) and triggers a burst that is then transmitted to downstream
426 premotoneuronal and motoneuronal populations. These processes can be regulated
427 independently by a variety of factors (double-headed arrows). Activation of µORs expressed in
428 $Dbx1^+$ neurons (left) slows the rhythm by decreasing excitability in $Dbx1^+$ neurons, reducing
429 synchrony, prolonging IBI, and reducing burstlet amplitude. SP (right) may mitigate the effects
430 of µOR activation by increasing *f* or reducing the threshold for burst generation.

431 **Experimental Procedures**

432 Experimental procedures were carried out in accordance with the United States Public Health
433 Service and Institute for Laboratory Animal Research Guide for the Care and Use of Laboratory
434 Animals. All protocols were approved by University of California Animal Research Committee
435 and the Rosalind Franklin University of Medicine and Science Institutional Animal Care and Use
436 Committee. Every effort was made to minimize pain and discomfort, as well as the number of
437 animals.

438 *Transgenic mice*

439 *Dbx1^{Cre}* mice (Bielle et al., 2005) were crossed with either *Rosa26^{tdTomato}* (JAX Stock No. 007908)
440 or *Oprm1$^{fl/fl}$* (Weibel et al., 2013) mouse lines. *Dbx1^{Cre};Rosa26^{tdTomato}* were used to visualize
441 Dbx1^{+} neurons, and *Dbx1^{Cre};Oprm1$^{fl/fl}$* mice were used to delete µORs selectively in Dbx1^{+}
442 neurons using cre-lox recombination. Animal genotypes were verified via real time polymerase
443 chain reaction using primers specific for the *Oprm1$^{fl/fl}$* conditional allele or cre recombinase
444 (Pierani et al., 2001; Rose et al., 2009; Weibel et al., 2013) or by direct visualization of
445 fluorescent reporter.

446 *Immunohistochemistry and confocal imaging*

447 *Dbx1^{Cre};Rosa26^{tdTomato}* and *Dbx1^{Cre};Oprm1$^{fl/fl}$* mice were anesthetized at P0-4 by inhalation of
448 isoflurane. The brainstem was isolated from the pons to the rostral cervical spinal cord, fixed in
449 4% paraformaldehyde, and cryoprotected in 30% sucrose before sectioned at 70mm thickness
450 using CRYOSTAR NX70 (Thermo Scientific). Tissue sections were washed in PBS, and incubated
451 in primary antibody at least overnight, followed by incubation in secondary antibody for 2 hrs at
452 room temperature, and cover-slipped in Vectashield with or without DAPI. Primary antibodies
453 used included rabbit anti-µOR (1:400), goat anti-ChAT (1:400, SCBT); Secondary antibodies were
454 species specific (1:250) and conjugated to Alexa 488, Rhodamine or Cy5 (Invitrogen or Jackson
455 ImmunoResearch). Sections were imaged using confocal laser scanning microscopy. Confocal
456 images were captured on a Zeiss LSM 710 Meta confocal microscope implemented on an
457 upright Axioplan 2 microscope. Zen software was used to capture images. Confocal images

458 were analyzed with ImageJ, and the final figures were composed in Adobe Photoshop and/or
459 Microsoft Powerpoint.

460 *In situ hybridization*

461 As described above, mice were anesthetized at P0-4 by inhalation of isoflurane. The isolated
462 brainstem was rapidly frozen in dry ice and stored at -80°C until sectioning. Transverse sections
463 (14-20 µm) were cut on a cryostat (CryoStar NX70, Thermo Scientific) and mounted on
464 SuperFrost Plus (Fisher Scientific) slides. Slides were processed for fluorescence *in situ*
465 hybridization of three target RNAs simultaneously according to manufacturer protocols for
466 RNAScope® (Advanced Cell Diagnostics). Briefly, fresh frozen tissue samples were postfixed in
467 10% neutral buffered formalin, washed, and dehydrated in sequential concentrations of
468 ethanol (50, 70 and 100%) at RT. Samples were treated with protease IV, then incubated for
469 two hours at 40°C in the presence of target probes to allow for hybridization. The following
470 target probes were used: Mm-Oprm1, Mm-Tac1, and Mm-ChAT. A series of three amplification
471 steps was necessary to provide substrates for target fluorophore labeling (ChAT conjugated to
472 fluorescein (1:1200), Oprm1 to Cy5, (1:1200) and Tac1 to Cy3 (1:1500) (Jackson
473 ImmunoResearch). After labeling, samples were counterstained with DAPI. ProLong® Gold
474 (Invitrogen), was applied to each slide prior to cover slipping. Images were acquired on a
475 confocal laser scanning microscope (LSM710 META, Zeiss). High-resolution z-stack confocal
476 images were taken at 0.3 µm intervals. Cell-by-cell µOR expression profiles were quantified in
477 selected regions of interest (TAC1 positive neurons in preBötC) according to a five-grade scoring
478 system recommended by the manufacturer (ACD score; 0, no staining; 1, 1-3 dots/cell; 2, 4-9
479 dots/cell; 3, 10-15 dots/cell; 4, >15 dots/cell), where a dot (>0.60 µm) represented a single RNA
480 transcript. A Histo score (H-score) was then calculated from the data, using image-based
481 software analysis (FIJI):

482 $$\mathrm{H-score} = \sum_{\substack{bin \\ 0-4}}^{n} (\text{ACD score x percentage of cells per bin})$$

483 *Slice preparation and electrophysiology*

484 Neonatal C57BL/6 or mutant mice (P0-5) of either sex were used for cutting brainstem
485 medullary transverse slices (550-600 µm thick) containing the rhythm-generating preBötC, XII
486 inspiratory motoneurons, and premotoneurons linking these populations (Koizumi et al., 2008;
487 Smith et al., 1991). To obtain slices with the preBötC at the surface, the rostral cut was made
488 above the first set of XII nerve rootlets at the level of the dorsomedial cell column and principal
489 lateral loop of the inferior olive, and the caudal cut captured the obex (Ruangkittisakul et al.,
490 2011). Slice cutting artificial cerebrospinal fluid (ACSF) solution was composed of (in mM): 124
491 NaCl, 3 KCl, 1.5 $CaCl_2$, 1 $MgSO_4$, 25 $NaHCO_3$, 0.5 NaH_2PO_4, and 30 D-glucose, equilibrated with
492 95% O_2 and 5% CO_2, 27°C, pH 7.4. Slices were placed rostral side up in a chamber and perfused
493 at 2-3 ml/min with 28-30°C recording ACSF. Baseline recording ACSF consisted of either the
494 cutting ACSF solution with K^+ raised to 9 mM and Ca^{2+} maintained at 1.5 mM (9/1.5 ACSF) for a
495 robust burst rhythm or the cutting ACSF solution with K^+ maintained at 3 mM and Ca^{2+} lowered
496 to 1 mM (3/1 ACSF) to study burstlets and bursts together (Kam et al., 2013a). Drugs, including
497 DAMGO, SP, picrotoxin, strychnine, and CdCl, were obtained from Sigma-Aldrich and bath-
498 applied at the specified concentrations. In all experiments, slices were allowed to equilibrate
499 for 30 min to ensure that the frequency and magnitude of XII and preBötC population activities
500 reached steady-state. Respiratory activity reflecting suprathreshold action potential firing from
501 populations of neurons was recorded from XII motor nucleus or nerve roots and as population
502 activity directly from the preBötC using suction electrodes (tip size ~50 µm) and an Axiopatch
503 200A (Molecular Devices), Multiclamp 700B (Molecular Devices), and/or a differential AC
504 amplifier (AM systems), filtered at 2–4 kHz, integrated, and digitized at 10 kHz. Integration was
505 performed on custom built Paynter filter with a 20-100 ms time constant. Digitized data were
506 analyzed off-line using custom procedures written for IgorPro (Wavemetrics).

507 *Holographic photostimulation*

508 Holographic photostimulation was performed on a Phasor SLM system (Intelligent Imaging
509 Innovations, Inc.) mounted around an epifluorescence upright microscope (Axioscope; Zeiss).
510 We used a 405 nm diode laser (CUBE 405-100; Coherent) to uncage MNI-glutamate (0.5 mM)
511 and depolarize targeted neurons. An iterative Fourier transform algorithm, implemented in

512 Slidebook 5 (Intelligent Imaging Innovations, Inc.), computed the phase pattern on the SLM
513 corresponding to the desired distribution of light intensity at the focal plane of the objective. A
514 blocker was inserted in the intermediate Fourier plane to block the unmodulated light
515 component (zero order spot) and replicate patterns (Golan et al., 2009). Neurons were targeted
516 by centering 10 um circular spots over the somata of the selected neurons. The laser intensity
517 per spot was set at 1-3 mW, which was previously determined to elicit bursts of action
518 potentials in the targeted neurons without the spread of glutamate to neighboring neurons
519 (Kam et al., 2013b). Each laser stimulation consisted of 5 x 0.8 ms pulses, delivered at 200 Hz. A
520 threshold stimulus was determined as the minimum number of neurons and minimum laser
521 power required to entrain preBötC bursts at slightly faster than the endogenous frequency with
522 a success rate > 80%. The latency between laser stimulation and burst initiation was calculated
523 as the time between the start of the next preBötC burst and the beginning of laser stimulation.
524 preBötC activity was used here, rather than XII activity, to isolate the effects of DAMGO on
525 rhythmogenic mechanisms and avoid additional delays or failures due to depression of XII
526 premotoneurons and motoneurons. Successful triggering of a burst by photostimulation was
527 defined as burst detection within 0.5 s of laser stimulation.

528 *Data analysis and statistics*

529 Semiautomated event detection of respiratory-related activity recorded in XII output or
530 preBötC population recordings was performed using custom procedures written in IgorPro.
531 Multiple criteria, including slope and amplitude thresholds, were used to select events
532 automatically, which were then confirmed visually. Event duration, amplitude, shape, and
533 synchrony between XII and preBötC activity were criteria used to categorize detected events as
534 burstlets, bursts, and doublets. Burstlets were events in preBötC that did not temporally
535 overlap a XII burst. Doublets were distinguished from bursts by their longer duration and the
536 presence of multiple peaks of activity. Two closely spaced bursts were considered a doublet
537 based on the distribution of the period of XII output. A small peak at <2 s in the distribution of
538 periods of XII bursts was usually observed. A Gaussian was fit to this small peak and a threshold
539 time interval was set. Two bursts separated by less than this threshold were considered a

540 doublet. As doublets were in phase with bursts and burstlets, these events were grouped with
541 bursts and not separately analyzed.

542 Rhythmogenic processes were captured by measuring the frequency of preBötC rhythmic
543 activity, which included small amplitude burstlets that were not transmitted to XII motor
544 output, larger amplitude bursts that produced XII bursts, and longer duration doublets that
545 were also transmitted to XII motoneurons. The average frequency was calculated as the mean
546 of the instantaneous frequencies (1/interevent interval) across all preBötC activity (burstlets,
547 bursts, and doublets) in that condition. Pattern generating processes that included the
548 production and transmission of preBötC activity to XII output were characterized by measuring
549 the fraction of preBötC events that were burstlets. The burstlet fraction was calculated as the
550 ratio of the number of burstlets to the total number of rhythmic preBötC events (burstlets,
551 bursts, and doublets). Amplitudes were normalized to the amplitude of the largest burst in the
552 control condition.

553 Data are expressed as mean ± SD. Comparisons between two groups were performed with
554 paired or unpaired Student's *t*-tests. Multiple comparisons were evaluated using parametric
555 one-way or two-way repeated measures ANOVA. Post-hoc Tukey or paired Student's *t*-tests
556 with the Bonferroni-Holm comparison were then used to determine significance for within
557 group comparisons. Statistical significance was set at $p < 0.05$.

558

559 **Supplemental Figure Legends**

560 **Figure S1. µOR, TAC1, and NK1R expression in preBötC.** Related to Figure 3.
561 (A) Confocal image of a medullary brainstem section at the level of the preBötC from a P2 wild
562 type mouse triple processed with RNAScope. Probes for NK1R (green), µOR (magenta), and
563 TAC1 (white) were used, and the tissue was counterstained with DAPI (blue). Scale bar, 20 µm.
564 (B) Higher magnification images showing colocalization of TAC1, NK1R, and µOR puncta in
565 several preBötC neurons (arrows) as well as a neuron that expressed NK1R and µOR, but not
566 TAC1 (arrowhead). Scale bar, 25 µm.

567 **Figure S2. Substance P increases preBötC *f* in *Dbx1^{Cre};Oprm1$^{fl/fl}$* mice.** Related to Figure 4.
568 (A) Representative traces showing ∫preBötC and ∫XII activity from a *Dbx1^{Cre};Oprm1$^{fl/fl}$* slice in
569 control (ctrl, left), 100 nM DAMGO (middle), and 500 nM Substance P (SP, right). Scale bar, 10 s.
570 (B) SP (500 nM) significantly increased preBötC *f* in slices from *Dbx1^{Cre};Oprm1$^{fl/fl}$* mice, while 100
571 nM DAMGO had no effect. *, $p < 0.05$, One-way ANOVA post-hoc Tukey test, n=4.

572 **References**

573 Ballanyi, K., and Ruangkittisakul, A. (2009). Structure-function analysis of rhythmogenic
574 inspiratory pre-Botzinger complex networks in "calibrated" newborn rat brainstem
575 slices. Respir Physiol Neurobiol 168, 158-178.
576 Bielle, F., Griveau, A., Narboux-Neme, N., Vigneau, S., Sigrist, M., Arber, S., Wassef, M., and
577 Pierani, A. (2005). Multiple origins of Cajal-Retzius cells at the borders of the developing
578 pallium. Nat Neurosci 8, 1002-1012.
579 Boom, M., Niesters, M., Sarton, E., Aarts, L., Smith, T.W., and Dahan, A. (2012). Non-analgesic
580 effects of opioids: opioid-induced respiratory depression. Curr Pharm Des 18, 5994-
581 6004.
582 Bouvier, J., Thoby-Brisson, M., Renier, N., Dubreuil, V., Ericson, J., Champagnat, J., Pierani, A.,
583 Chedotal, A., and Fortin, G. (2010). Hindbrain interneurons and axon guidance signaling
584 critical for breathing. Nat Neurosci 13, 1066-1074.
585 CBHSQ (2018). 2017 National Survey on Drug Use and Health: Detailed Tables. Rockville, MD:
586 Substance Abuse and Mental Health Services Administration.
587 Davies, J., and Dray, A. (1977). Substance P and opiate receptors. Nature 268, 351-352.
588 Del Negro, C.A., Kam, K., Hayes, J.A., and Feldman, J.L. (2009). Asymmetric control of inspiratory
589 and expiratory phases by excitability in the respiratory network of neonatal mice in
590 vitro. J Physiol 587, 1217-1231.
591 Fukazawa, Y., Maeda, T., Kiguchi, N., Tohya, K., Kimura, M., and Kishioka, S. (2007). Activation of
592 spinal cholecystokinin and neurokinin-1 receptors is associated with the attenuation of
593 intrathecal morphine analgesia following electroacupuncture stimulation in rats. J
594 Pharmacol Sci 104, 159-166.
595 Golan, L., Reutsky, I., Farah, N., and Shoham, S. (2009). Design and characteristics of
596 holographic neural photo-stimulation systems. J Neural Eng 6, 066004.
597 Gray, P.A., Hayes, J.A., Ling, G.Y., Llona, I., Tupal, S., Picardo, M.C., Ross, S.E., Hirata, T., Corbin,
598 J.G., Eugenin, J., and Del Negro, C.A. (2010). Developmental origin of preBotzinger
599 complex respiratory neurons. J Neurosci 30, 14883-14895.
600 Gray, P.A., Janczewski, W.A., Mellen, N., McCrimmon, D.R., and Feldman, J.L. (2001). Normal
601 breathing requires preBotzinger complex neurokinin-1 receptor-expressing neurons. Nat
602 Neurosci 4, 927-930.
603 Gray, P.A., Rekling, J.C., Bocchiaro, C.M., and Feldman, J.L. (1999). Modulation of respiratory
604 frequency by peptidergic input to rhythmogenic neurons in the preBotzinger complex.
605 Science 286, 1566-1568.
606 Hayes, J.A., Kottick, A., Picardo, M.C.D., Halleran, A.D., Smith, R.D., Smith, G.D., Saha, M.S., and
607 Del Negro, C.A. (2017). Transcriptome of neonatal preBotzinger complex neurones in
608 Dbx1 reporter mice. Sci Rep 7, 8669.
609 Janczewski, W.A., Onimaru, H., Homma, I., and Feldman, J.L. (2002). Opioid-resistant
610 respiratory pathway from the preinspiratory neurones to abdominal muscles: in vivo
611 and in vitro study in the newborn rat. J Physiol 545, 1017-1026.
612 Janczewski, W.A., Tashima, A., Hsu, P., Cui, Y., and Feldman, J.L. (2013). Role of inhibition in
613 respiratory pattern generation. J Neurosci 33, 5454-5465.

614 Johnson, S.M., Smith, J.C., and Feldman, J.L. (1996). Modulation of respiratory rhythm in vitro:
615 role of Gi/o protein-mediated mechanisms. J Appl Physiol (1985) 80, 2120-2133.
616 Kam, K., Worrell, J.W., Janczewski, W.A., Cui, Y., and Feldman, J.L. (2013a). Distinct inspiratory
617 rhythm and pattern generating mechanisms in the preBotzinger complex. J Neurosci 33,
618 9235-9245.
619 Kam, K., Worrell, J.W., Ventalon, C., Emiliani, V., and Feldman, J.L. (2013b). Emergence of
620 population bursts from simultaneous activation of small subsets of preBötzinger
621 complex inspiratory neurons. J Neurosci 33, 3332-3338.
622 Kibaly, C., Xu, C., Cahill, C.M., Evans, C.J., and Law, P.Y. (2019). Non-nociceptive roles of opioids
623 in the CNS: opioids' effects on neurogenesis, learning, memory and affect. Nat Rev
624 Neurosci 20, 5-18.
625 Koizumi, H., Wilson, C.G., Wong, S., Yamanishi, T., Koshiya, N., and Smith, J.C. (2008). Functional
626 imaging, spatial reconstruction, and biophysical analysis of a respiratory motor circuit
627 isolated in vitro. J Neurosci 28, 2353-2365.
628 Kream, R.M., Kato, T., Shimonaka, H., Marchand, J.E., and Wurm, W.H. (1993). Substance P
629 markedly potentiates the antinociceptive effects of morphine sulfate administered at
630 the spinal level. Proc Natl Acad Sci U S A 90, 3564-3568.
631 Lalley, P.M., Pilowsky, P.M., Forster, H.V., and Zuperku, E.J. (2014). CrossTalk opposing view:
632 The pre-Botzinger complex is not essential for respiratory depression following systemic
633 administration of opioid analgesics. J Physiol 592, 1163-1166.
634 Le Merrer, J., Becker, J.A., Befort, K., and Kieffer, B.L. (2009). Reward processing by the opioid
635 system in the brain. Physiol Rev 89, 1379-1412.
636 Lu, B., Su, Y., Das, S., Liu, J., Xia, J., and Ren, D. (2007). The neuronal channel NALCN contributes
637 resting sodium permeability and is required for normal respiratory rhythm. Cell 129,
638 371-383.
639 Mansour, A., Khachaturian, H., Lewis, M.E., Akil, H., and Watson, S.J. (1988). Anatomy of CNS
640 opioid receptors. Trends Neurosci 11, 308-314.
641 Manzke, T., Guenther, U., Ponimaskin, E.G., Haller, M., Dutschmann, M., Schwarzacher, S., and
642 Richter, D.W. (2003). 5-HT4(a) receptors avert opioid-induced breathing depression
643 without loss of analgesia. Science 301, 226-229.
644 Montandon, G., and Horner, R. (2014). CrossTalk proposal: The preBotzinger complex is
645 essential for the respiratory depression following systemic administration of opioid
646 analgesics. J Physiol 592, 1159-1162.
647 Montandon, G., Qin, W., Liu, H., Ren, J., Greer, J.J., and Horner, R.L. (2011). PreBotzinger
648 complex neurokinin-1 receptor-expressing neurons mediate opioid-induced respiratory
649 depression. J Neurosci 31, 1292-1301.
650 Montandon, G., Ren, J., Victoria, N.C., Liu, H., Wickman, K., Greer, J.J., and Horner, R.L. (2016).
651 G-protein-gated Inwardly Rectifying Potassium Channels Modulate Respiratory
652 Depression by Opioids. Anesthesiology 124, 641-650.
653 Phillips, R.S., Cleary, D.R., Nalwalk, J.W., Arttamangkul, S., Hough, L.B., and Heinricher, M.M.
654 (2012). Pain-facilitating medullary neurons contribute to opioid-induced respiratory
655 depression. J Neurophysiol 108, 2393-2404.
656 Picardo, M.C.D., Sugimura, Y.K., Dorst, K.E., Kallurkar, P.S., Akins, V.T., Ma, X., Teruyama, R.,
657 Guinamard, R., Kam, K., Saha, M.S., and Del Negro, C.A. (2019). Trpm4 ion channels in

658 pre-Botzinger complex interneurons are essential for breathing motor pattern but not
659 rhythm. PLoS Biol 17, e2006094.
660 Pierani, A., Moran-Rivard, L., Sunshine, M.J., Littman, D.R., Goulding, M., and Jessell, T.M.
661 (2001). Control of interneuron fate in the developing spinal cord by the progenitor
662 homeodomain protein Dbx1. Neuron 29, 367-384.
663 Pokorski, M., and Lahiri, S. (1981). Effects of naloxone on carotid body chemoreception and
664 ventilation in the cat. J Appl Physiol Respir Environ Exerc Physiol 51, 1533-1538.
665 Prkic, I., Mustapic, S., Radocaj, T., Stucke, A.G., Stuth, E.A., Hopp, F.A., Dean, C., and Zuperku,
666 E.J. (2012). Pontine mu-opioid receptors mediate bradypnea caused by intravenous
667 remifentanil infusions at clinically relevant concentrations in dogs. J Neurophysiol 108,
668 2430-2441.
669 Ren, J., and Greer, J.J. (2006). Modulation of respiratory rhythmogenesis by chloride-mediated
670 conductances during the perinatal period. J Neurosci 26, 3721-3730.
671 Rose, M.F., Ren, J., Ahmad, K.A., Chao, H.T., Klisch, T.J., Flora, A., Greer, J.J., and Zoghbi, H.Y.
672 (2009). Math1 is essential for the development of hindbrain neurons critical for
673 perinatal breathing. Neuron 64, 341-354.
674 Ruangkittisakul, A., Panaitescu, B., and Ballanyi, K. (2011). K(+) and Ca(2)(+) dependence of
675 inspiratory-related rhythm in novel "calibrated" mouse brainstem slices. Respir Physiol
676 Neurobiol 175, 37-48.
677 Schmidt, Y., Gaveriaux-Ruff, C., and Machelska, H. (2013). mu-Opioid receptor antibody reveals
678 tissue-dependent specific staining and increased neuronal mu-receptor
679 immunoreactivity at the injured nerve trunk in mice. PLoS One 8, e79099.
680 Shao, X.M., and Feldman, J.L. (1997). Respiratory rhythm generation and synaptic inhibition of
681 expiratory neurons in pre-Botzinger complex: differential roles of glycinergic and
682 GABAergic neural transmission. J Neurophysiol 77, 1853-1860.
683 Smith, J.C., Ellenberger, H.H., Ballanyi, K., Richter, D.W., and Feldman, J.L. (1991). Pre-Botzinger
684 complex: a brainstem region that may generate respiratory rhythm in mammals. Science
685 254, 726-729.
686 Stucke, A.G., Miller, J.R., Prkic, I., Zuperku, E.J., Hopp, F.A., and Stuth, E.A. (2015). Opioid-
687 induced Respiratory Depression Is Only Partially Mediated by the preBotzinger Complex
688 in Young and Adult Rabbits In Vivo. Anesthesiology 122, 1288-1298.
689 Tan, W., Pagliardini, S., Yang, P., Janczewski, W.A., and Feldman, J.L. (2010). Projections of
690 preBotzinger complex neurons in adult rats. J Comp Neurol 518, 1862-1878.
691 van der Schier, R., Roozekrans, M., van Velzen, M., Dahan, A., and Niesters, M. (2014). Opioid-
692 induced respiratory depression: reversal by non-opioid drugs. F1000Prime Rep 6, 79.
693 Wang, X., Hayes, J.A., Revill, A.L., Song, H., Kottick, A., Vann, N.C., LaMar, M.D., Picardo, M.C.,
694 Akins, V.T., Funk, G.D., and Del Negro, C.A. (2014). Laser ablation of Dbx1 neurons in the
695 pre-Botzinger complex stops inspiratory rhythm and impairs output in neonatal mice.
696 Elife 3, e03427.
697 Weibel, R., Reiss, D., Karchewski, L., Gardon, O., Matifas, A., Filliol, D., Becker, J.A., Wood, J.N.,
698 Kieffer, B.L., and Gaveriaux-Ruff, C. (2013). Mu opioid receptors on primary afferent
699 nav1.8 neurons contribute to opiate-induced analgesia: insight from conditional
700 knockout mice. PLoS One 8, e74706.

701 Williams, J.T., Christie, M.J., and Manzoni, O. (2001). Cellular and synaptic adaptations
702 mediating opioid dependence. Physiol Rev 81, 299-343.
703 Yeh, S.Y., Huang, W.H., Wang, W., Ward, C.S., Chao, E.S., Wu, Z., Tang, B., Tang, J., Sun, J.J.,
704 Esther van der Heijden, M.*, et al.* (2017). Respiratory Network Stability and Modulatory
705 Response to Substance P Require Nalcn. Neuron 94, 294-303 e294.
706 Zhang, Z., Xu, F., Zhang, C., and Liang, X. (2007). Activation of opioid mu receptors in caudal
707 medullary raphe region inhibits the ventilatory response to hypercapnia in anesthetized
708 rats. Anesthesiology 107, 288-297.
709 Zhang, Z., Zhuang, J., Zhang, C., and Xu, F. (2011). Activation of opioid mu-receptors in the
710 commissural subdivision of the nucleus tractus solitarius abolishes the ventilatory
711 response to hypoxia in anesthetized rats. Anesthesiology 115, 353-363.
712
713

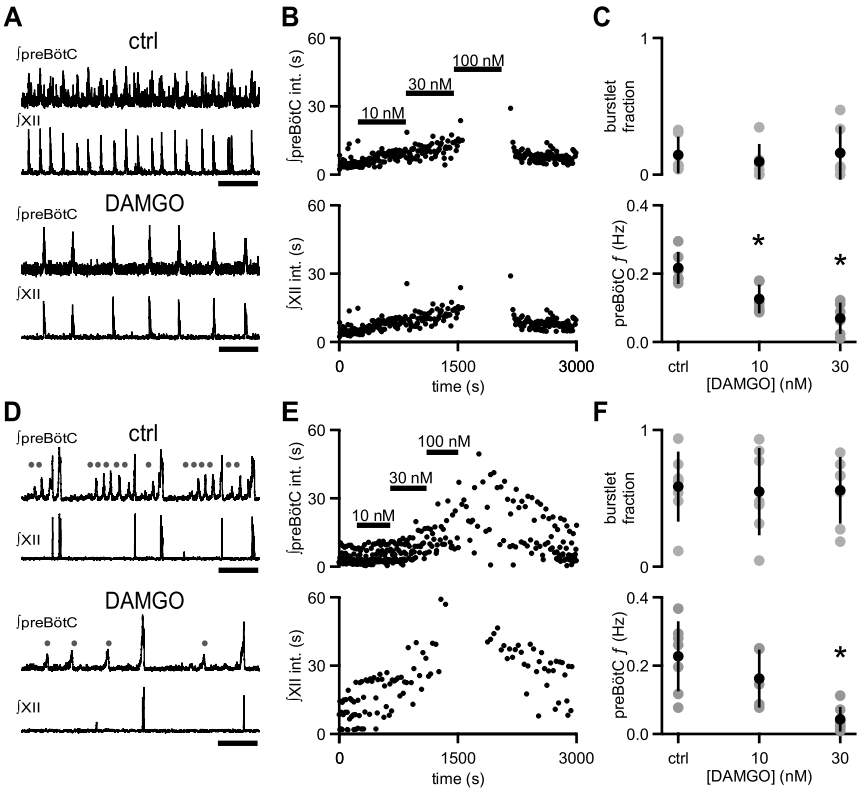
A
ctrl
∫preBötC
∫XII
DAMGO
∫preBötC
∫XII
B
∫preBötC int. (s)
10 nM
30 nM
100 nM
∫XII int. (s)
time (s)
C
burstlet fraction
preBötC f (Hz)
[DAMGO] (nM)
ctrl
D
ctrl
∫preBötC
∫XII
DAMGO
∫preBötC
∫XII
E
∫preBötC int. (s)
10 nM
30 nM
100 nM
∫XII int. (s)
time (s)
F
burstlet fraction
preBötC f (Hz)
[DAMGO] (nM)
ctrl

Figure 1

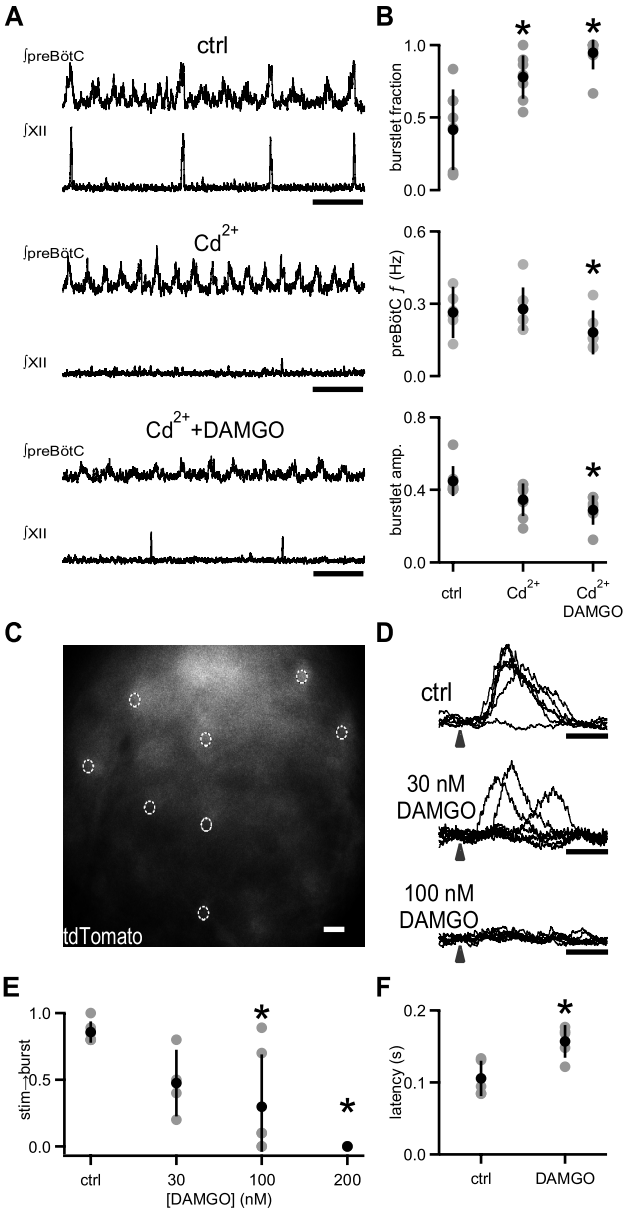
A
ctrl
∫preBötC
∫XII
Cd2+
Cd2+ +DAMGO
B
burstlet fraction
preBötC f (Hz)
burstlet amp.
ctrl
Cd2+
Cd2+ DAMGO
C
tdTomato
D
ctrl
30 nM DAMGO
100 nM DAMGO
E
stim→burst
[DAMGO] (nM)
F
latency (s)
DAMGO

Figure 2

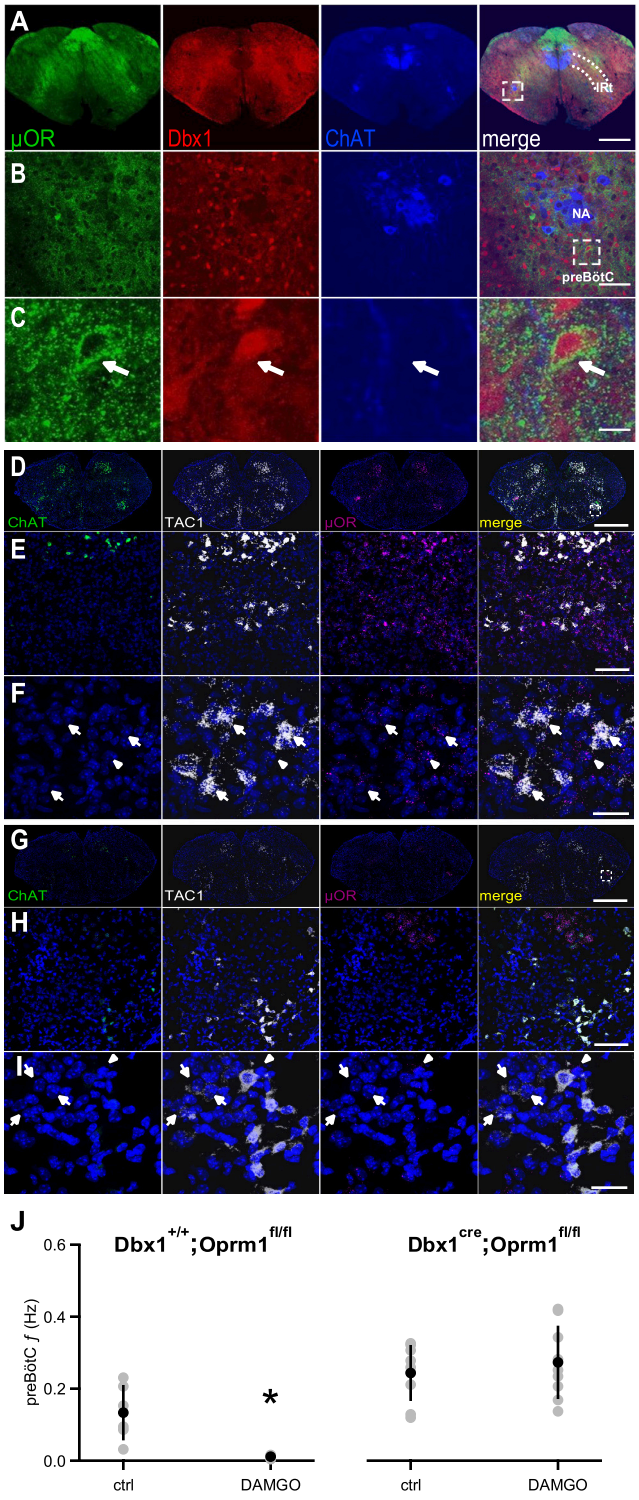
A
μOR
Dbx1
ChAT
merge
Rt
B
NA
preBötC
C
D
ChAT
TAC1
μOR
merge
E
F
G
ChAT
TAC1
μOR
merge
H
I
J
Dbx1+/+;Oprm1fl/fl
Dbx1cre;Oprm1fl/fl
preBötC f (Hz)
0.6
0.4
0.2
0.0
*
ctrl
DAMGO
ctrl
DAMGO

Figure 3

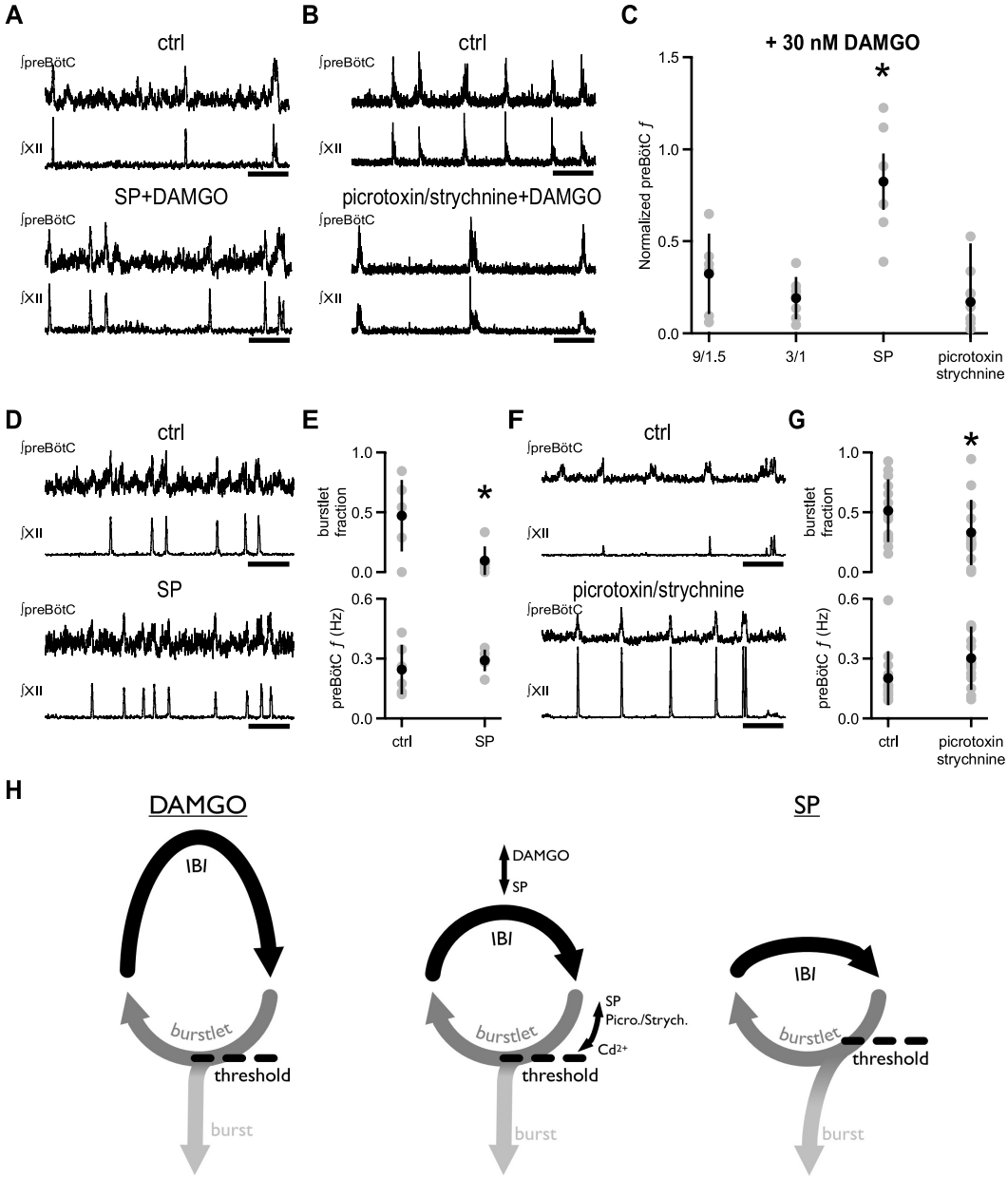
A
ctrl
∫preBötC
∫XII
SP+DAMGO
B
ctrl
picrotoxin/strychnine+DAMGO
C
+ 30 nM DAMGO
Normalized preBötC f
9/1.5
3/1
SP
picrotoxin strychnine
D
SP
E
burstlet fraction
preBötC f (Hz)
F
picrotoxin/strychnine
G
H
DAMGO
SP
IBI
burstlet
threshold
burst
Picro./Strych.
Cd2+

Figure 4